We clearly observed highly ordered crystalline structures in the supernatant sample collected after centrifugation of the ZnO suspension (see ESI, Fig. S3†), but no crystalline structure was detected in the controls, in which the solution did not contain ZnO NPs. Together with X-ray diffraction (XRD) characteristics of the ZnO NPs (see ESI, Fig. S4†) and the EDS elemental mapping in ref. 10, these data indicate that the highly ordered structures are the ZnO NPs contained in the supernatant; individual ZnO NPs (Fig. 2b and ESI, Fig. S3†) are even embedded inside the clusters formed by ZnO NPs adsorbing various components from the biological environment.

In addition, we detected particles with different sizes in the supernatants collected after various centrifugation conditions, including the very harsh centrifugation conditions of 150 000 × *g* for 60 min (see ESI, Table S1†), by DLS measurement. For a control DLS measurement, we did not detect any particle in the solvents used for dispersing NPs at room temperature, suggesting that no protein sediment was formed under the experimental conditions (see ESI, Table S1†). Note that if the medium with FBS is incubated in a cell culture environment, particle-shaped matters can be formed (see ESI, Fig. S1†), and thus can influence the size distribution of NMs characterized by DLS. From the DLS results, clusters as large as 1.6 μm even existed in the supernatant generated at 20 000 × *g* for 20 min. It is well known that DLS measures the Brownian motion of NPs and relates this movement to an equivalent hydrodynamic diameter, with the motion of smaller particles not being easily detected or being overestimated. The measurement data are also influenced by time-dependent sedimentation and agglomeration/aggregation of NPs in order to reduce the surface energy in a medium. DLS is an indirect method for calculation of size by means of a physical model. This requires information on the refractive index of the dispersant in which the NMs are dispersed. Such a refractive index is now absent. All these factors suggest that the calculated equivalent hydrodynamic diameters are not compared with the particle sizes measured by TEM. Despite the problem of the DLS technique, our results suggest the presence of ZnO NPs in the supernatants. On the other hand, different from the DLS data, the maximum size of ZnO remaining in the supernatant observed by TEM is only around 100 nm, and only a few of such-sized clusters were found by searching the whole sample. The comparison of the size information measured by DLS and TEM suggests that the different size results can be obtained by different analytical techniques. Furthermore, the observation of remaining ZnO particles of size up to 100 nm indicates that the ZnO NPs in the supernatant may not be the portion of very small ZnO particles in the suspension. Despite the origin of the remaining ZnO clusters from either small particles or large clusters, their existence in the supernatant suggests that the ZnO NPs were not completely removed by the centrifugation process, which was at much harsher conditions than those used for the estimation of released metallic ions.[8]

3.2 Zn elemental concentration in supernatant

Zn concentrations of the supernatants produced by different centrifugation conditions were measured by using ICP-OES. As summarized in Table 1, the percentage of NPs removed from a suspension is dependent more on the relative centrifugal force than on centrifugation time. In the case of 60 nm sized ZnO NPs, at a relative centrifugal force of 20 000 × *g*, about 23.6% of the ZnO NPs were removed from a 25 μg mL^{-1} suspension, while 34.1% were removed at 150 000 × *g*. Extending the centrifugation time from 20 to 60 min at either 20 000 × *g* or 150 000 × *g* did not significantly change the percentage of ZnO NPs removed from the suspension. For instance, the Zn concentrations of the supernatants collected after centrifugation of the initial ZnO suspension for 20 min and 60 min at 20 000 × *g* were 16.8 and 16.9 ppm, respectively. However, the fraction removed at a fixed centrifugation time and fixed centrifugal force depended on the initial concentration of the nanoparticle suspension. About 50% of the ZnO NPs were removed from the 50 μg mL^{-1} suspension, which might be due to easy aggregation at a higher concentration to form larger aggregates. We obtained similar results to the 60 nm sized ZnO NPs when the 20 nm sized ZnO NPs were used for investigation. For both 60 nm and 20 nm sized ZnO NPs, we also studied the influence of FBS on the concentration of elemental Zn in the supernatant (Table 1), and found that the FBS with a volume ratio of 10% to the medium had no obvious effect on the removal of ZnO NPs.

In previous nanotoxicity studies that accounted for the metallic ion effect on cytotoxicity,[8,12–14,19,20,22–24] the elemental Zn concentration of supernatant obtained by ICP-MS relevant techniques was assumed to be the free Zn^{2+} ion concentration released in cell culture medium. However, it should be noted that the elemental concentration obtained by ICP-MS relevant techniques[25,26] can be affected by free ions and by the ions that result from decomposition of matter at the very high temperature and/or acid environments present for an ICP-MS measurement. That is, after the sample is injected for ICP-MS measurement, the plasma's extreme temperature or strong acid causes the sample to separate into individual atoms (atomization); and then these atoms are ionized ($M \rightarrow M^{+} + e^{-}$) so that they can be detected by the mass spectrometer. As a result, the digestion procedures involved in ICP-MS relevant techniques make it almost impossible to differentiate the ions formed as a result of nanomaterial dissolution from the NMs *per se*. Therefore, our TEM observation (Fig. 2) and DLS result (see ESI, Tables S1 and S2†) clearly suggest that the Zn concentration as measured by ICP-MS relevant techniques cannot be considered to be the actual concentration of free Zn^{2+} ions released in cell culture medium, as the centrifugation process does not completely remove ZnO NPs from the suspension. Our finding suggests the urgent need to establish relevant characterization method for accurate measurement of free ions in solution for toxicity study.

3.3 Toxic contribution of potentially released Zn^{2+}

To evaluate the toxicity of Zn^{2+} ions released into the cell culture medium, we investigated the viability of A549 cells after exposure to the supernatant collected after centrifugation of the ZnO suspension in medium containing FBS. We first investigated

Table 1 Elemental concentrations determined by ICP-OES

Sample	Centrifugation condition: Force (× *g*)	Centrifugation condition: Time (min)	Al ppm (m/v) (μg mL^{-1})	Zn ppm (m/v) (μg mL^{-1})
ZnO suspension[a]	None		0	22.0
ZnO suspension[b]	None		0	22.3
ZnO supernatant[c]	20 000	20	0	16.8
	20 000	60	0	16.9
	150 000	20	0	14.5
	150 000	60	0	14.5
ZnO supernatant[d]	150 000	60	0	14.7
ZnO supernatant[e]	20 000	20	0	25.1
Al-doped ZnO suspension[f]	None		<0.1	20.0
Al-doped ZnO supernatant[g]	20 000	60	0	12.8
ZnO suspension[h]	None		0	21.8
ZnO suspension[i]	None		0	21.6
ZnO supernatant[j]	150 000	60	0	14.3
ZnO supernatant[k]	150 000	60	0	14.5

[a] Prepared by dispersing 60 nm ZnO NPs (about 25 μg mL^{-1}) in medium with FBS. [b] Prepared by dispersing 60 nm ZnO NPs (about 25 μg mL^{-1}) in medium without FBS. [c] Collected after centrifugation of the ZnO (60 nm NPs) suspension (about 25 μg mL^{-1}) in medium with FBS. [d] Collected after centrifugation of the ZnO (60 nm NPs) suspension (about 25 μg mL^{-1}) in medium without FBS. [e] Collected after centrifugation of the ZnO (60 nm NPs) suspension (about 50 μg mL^{-1}) in medium with FBS. [f] Prepared by dispersing Al-doped ZnO NPs (50 nm NPs, about 25 μg mL^{-1}) in medium with FBS. [g] Collected after centrifugation of the Al-doped ZnO NP (50 nm NPs, about 25 μg mL^{-1}) suspension in medium with FBS. [h] Prepared by dispersing ~20 nm ZnO NPs (about 25 μg mL^{-1}) in medium with FBS. [i] Prepared by dispersing ~20 nm ZnO NPs (about 25 μg mL^{-1}) in medium without FBS. [j] Collected after centrifugation of the ZnO (20 nm NPs) suspension (about 25 μg mL^{-1}) in medium with FBS. [k] Collected after centrifugation of the ZnO (20 nm NPs) suspension (about 25 μg mL^{-1}) in medium without FBS.

the cytotoxicity of ZnO NP suspension as a function of the suspension concentration. The A549 cell viability (Fig. 3) suggests that there is no obvious toxic effect if the concentration of ZnO NP suspension is not higher than 25 μg mL^{-1}; the 25 μg mL^{-1} suspension exhibited a toxic effect but not statistically important ($p < 0.05$). As shown in Fig. 4, the supernatant with an elemental Zn concentration of 25.1 ppm (Table 1), collected after the centrifugation of the ZnO NP suspension with a concentration of 50 μg mL^{-1}, had no obviously toxic effects on A549 cells during the exposure period of 24 h (Fig. 4a, d and f), *i.e.*, having a viability of about 95%. This observation is different from that of the 25 μg mL^{-1} suspension (Fig. 3), in which possibly dissolved Zn^{2+} ions were present together with ZnO

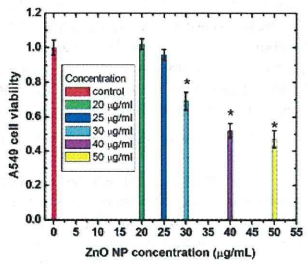

Fig. 3 A549 cell viability as a function with concentration of ZnO NP suspension of DMEM medium with FBS for 24 h exposure.

NPs. Furthermore, the observation is quite different from that of the 50 μg mL^{-1} ZnO NP suspension that seriously affected the cell viability (Fig. 4c). If we assumed all the 25.1 ppm, *i.e.*, 25.1 μg mL^{-1}, Zn as the free Zn^{2+} ions, these Zn^{2+} ions could cause about 5% cell death. Considering the exposure of the 50 μg mL^{-1} ZnO NP suspension (25.1 μg mL^{-1} was assumed as free Zn^{2+}) caused about 50% cell death, we found that about 90% of the dead cells were due to the other 24.9 μg mL^{-1} ZnO NPs. The analysis also indicates that the cytotoxicity was not a function of the concentration of fractions of the Zn element. Although the question is not so simple, this hypothesis reflects that the maximum toxic contribution of released Zn^{2+} ions to the cells was only about 10%. Thus, the above results suggest that free Zn cation in the cell culture medium had a negligible contribution to the cytotoxicity as compared to the non-dissolved ZnO NPs, which is in line with the other reports.[17,28] On the other hand, the addition of FBS to the medium had a remarkable influence on cell viability due to the growth factors contained in FBS (Fig. 4b and e). However, as compared to the toxic effect of ZnO NPs, the FBS function became negligible (Fig. 4c–e). Although Zn^{2+} ions are known to interact with proteins and serum albumin transports Zn^{2+} ions, the reasons for the negligible effect of the FBS might be absence of sufficient free Zn^{2+} ions and/or complicated interaction of the ZnO NPs in the biological environment.[9,10]

We previously reported that Al-doped ZnO NPs are more toxic than non-doped ZnO NPs and attributed the cytotoxic effects of the Al dopant to the enhancement of electrical conduction of ZnO.[27] Here, we find that the elemental Zn concentration (12.8 ppm) of the Al-doped ZnO suspension

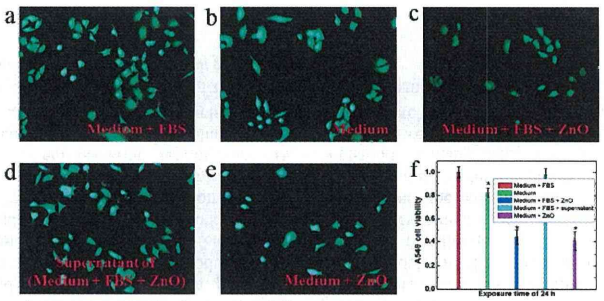

Fig. 4 Viability of A549 cells after 24 h exposure to ZnO NPs in different biological environments. (a)–(e) Live cell fluorescence images. (a) Control experiment, where A549 cells were exposed to medium supplemented with FBS but without ZnO NPs. (b) Control experiment, where A549 cells were exposed to medium without FBS and without ZnO NPs. (c) A549 cells exposed to ZnO NP suspension (50 μg mL^{-1}) in medium with FBS. (d) A549 cells exposed to the supernatant collected after centrifugation of the ZnO NP suspension (50 μg mL^{-1}) in medium with FBS. (e) A549 cells exposed to ZnO NPs suspension (50 μg mL^{-1}) in medium without FBS. (f) Statistical analysis of cell viability. *Denotes significance in comparison to control values ($p < 0.05$).

supernatant was lower than that of the non-doped ZnO supernatant (16.9 ppm) (Table 1). If we normalized a percentage of the total Zn concentration in the samples, the elemental Zn concentration of the Al-doped ZnO supernatant was about 13.3 ppm, remaining lower than that of non-doped ZnO supernatant. Together with a previous study,[27] this result suggests that the toxic effect of the Al-doped ZnO NPs and the non-doped ZnO NPs was not proportional to the concentration of elemental Zn in the samples, consistent with the above analysis. The independence of the cytotoxicity on the concentration of elemental Zn is in good agreement with the finding of Moos *et al.*,[17] that is, the cytotoxicity of ZnO NPs to RKO human colon carcinoma cells was not dependent on the Zn^{2+} concentration in the cell culture medium. Therefore, Zn ions in the medium are not the main cause of the observed cytotoxicity.[17,28,29] Also, there is no strong evidence whether the uptake of Zn^{2+} or ZnO NPs was the dominant pathway for internalizing zinc[16] or its toxic effect. Our result with the Al-doped ZnO NPs is in contrast to that of iron-doped ZnO NPs,[30] in which the reduced toxicity of iron-doped ZnO NPs, compared with ZnO NPs, was attributed to the lower solubility of the iron-doped ZnO NPs than ZnO NPs based on the analysis of Zn elemental concentration measured by ICP-MS. However, as discussed above, the concentration of free Zn^{2+} ion in supernatants could actually be lower than the data obtained by ICP-MS due to the difficulty to completely remove non-dissolved NPs. Thus, the assumption of elemental concentration as free ion concentration could overestimate the contribution of free metal ions to adverse biological effects.

If sufficient Zn^{2+} ions are present either outside or inside cells, it can certainly cause adverse effect on cells due to various mechanisms such as disruption of cellular Zn homeostasis. The question is how much ZnO NP can be dissolved in the cell culture medium. In general, the solubility of metal oxides is highly dependent on the pH of the solution,[15] where the oxides are dispersed, and the method used to disperse the oxides. ZnO and CuO is nearly insoluble in de-ionized water and in an extracellular solution,[15,19] but solubility increases in acidic environments[31] and in the presence of chelators.[19] Although there is still no direct and reliable technique for measuring the concentrations of free ions in a suspension,[32–34] we have demonstrated a protocol here for determining whether there are non-dissolved NPs in a collected supernatant, highlighting the need to establish relevant characterization techniques. Also, a simple comparison of toxicity between NPs and the solution of metal salts[14,21] such as $ZnCl_2$ and $ZnNO_3$ is not enough to elucidate the potential ill effects of NPs because of the variety of local biological environments, such as pH value, between NPs and salt solutions.[19]

The above analysis clarifies the contribution of free Zn^{2+} ions to the observed cytotoxicity and suggests that there are other dominant factors contributing to the cytotoxicity. One of the factors is the electronic properties[2,20,24,35] of nano-oxides. There are singular evidences showing the influence of the electronic properties of metal oxides[20,24] and carbon nanotubes[35] on toxicological potential[36] at cellular and whole animal levels since our work.[27] Furthermore, electronic properties have been recently developed as a paradigm for predicting the generation of oxidative stress and acute pulmonary inflammation associated with metal oxides.[20]

4 Conclusions

We found that it is difficult to completely remove ZnO NPs dispersed in a cell culture medium by centrifugation, leading to the overestimation of the concentration of free ions when determined by ICP-MS relevant techniques. We also showed that the cytotoxicity of ZnO NPs is not proportional to the concentration of Zn elemental concentration. The maximum toxic contribution of released free Zn^{2+} ions to the A549 cell lines was estimated to be about 10%. Our results indicate that other factors including electronic properties of the ZnO NPs, rather than the Zn concentration, play a dominant role in the cytotoxicity, and identification of the key physicochemical characteristics of NMs which govern the potential toxic effect remains a challenge.

Acknowledgements

This work was partially supported by the National Natural Science Foundation of China (no. 51011130028, 50990063 and 50973095), by Zhejiang Provincial Natural Science Foundation of China (Youth Talent Program: R4110030), Science and Technology Department of Zhejiang Provincial (Qianjiang Talent Program: 2011R10077), by Program for New Century Excellent Talents in University (NCET-12-0494) and by the Interdisciplinary Laboratory for Nanoscale Science and Technology of National Institute for Materials Science (NIMS), Japan. We thank S. Takenouchi at the chemical analysis station for assistance with ICP-OES measurements, and Y. Nemoto and H. Gao for assistance with TEM measurements.

References

1 D. Y. Lai, *Wiley Interdiscip. Rev.: Nanomed. Nanobiotechnol.*, 2012, **4**, 1–15.
2 N. Hanagata, F. Zhuang, S. Connolly, J. Li, N. Ogawa and M. S. Xu, *ACS Nano*, 2011, **5**, 9326–9338.
3 A. Galeone, G. Vecchio, M. A. Malvindi, V. Brunetti, R. Cingolani and P. P. Pompa, *Nanoscale*, 2012, **4**, 6401–6407.
4 A. D. Maynard, D. B. Warheit and M. A. Philbert, *Toxicol. Sci.*, 2011, **120**, S109–S129.
5 H. F. Krug and P. Wick, *Angew. Chem., Int. Ed.*, 2011, **50**, 1260–1278.
6 J. K. Jiang, G. Oberdörster and P. Biswas, *J. Nanopart. Res.*, 2009, **11**, 77–89.
7 W. J. Stark, *Angew. Chem., Int. Ed.*, 2011, **50**, 1242–1258.
8 T. Xia, M. Kovochich, M. Liong, L. Madler, B. Gilbert, H. Shi, J. I. Yeh, J. I. Zink and A. E. Nel, *ACS Nano*, 2008, **2**, 2121–2134.
9 M. S. Ehrenberg, A. E. Friedman, J. A. N. Finkelstein, G. Oberdörster and J. McGrath, *Biomaterials*, 2009, **30**, 603–610.
10 M. S. Xu, J. Li, H. Iwai, Q. S. Mei, D. Fujita, H. X. Su and N. Hanagata, *Sci. Rep.*, 2012, **2**, 406.
11 R. J. Vandebriel and W. H. De Jong, *Nanotechnol., Sci. Appl.*, 2012, **5**, 61–71.
12 T. J. Brunner, P. Wick, P. Manser, P. Spohn, R. N. Grass, L. K. Limbach, A. Brunink and W. J. Stark, *Environ. Sci. Technol.*, 2006, **40**, 4374–4381.
13 N. N. Franklin, N. J. Rogers, S. C. Apte, G. E. Batley, G. E. Gadd and P. S. Casey, *Environ. Sci. Technol.*, 2007, **41**, 8484–8490.
14 X. Y. Deng, Q. X. Luan, W. T. Chen, Y. L. Wang, M. H. Wu, H. J. Zhang and Z. Jiao, *Nanotechnology*, 2009, **20**, 115101.
15 M. H. Muller, J. Kulkarni, M. Motskin, A. Goode, P. Winship, J. N. Skepper, M. P. Ryan and A. Porter, *ACS Nano*, 2010, **4**, 6767–6779.
16 B. Gilbert, S. C. Fakra, T. Xia, S. Pokhrel, L. Madler and A. E. Nel, *ACS Nano*, 2012, **6**, 4921–4930.
17 P. J. Moos, K. Chung, D. Woessner, M. Honeggar, N. Shane Cutler and J. M. Veranth, *Chem. Res. Toxicol.*, 2010, **23**, 733–739.
18 A. M. Studer, L. K. LimbachK, L. Van Duc, F. Krumeich, E. K. Athanassiou, L. C. Gerber, H. Moch and W. J. Stark, *Toxicol. Lett.*, 2010, **197**, 169–174.
19 C. Gunawan, W. Y. Teoh, C. P. Marquis and R. Amal, *ACS Nano*, 2011, **5**, 7214–7225.
20 H. Y. Zhang, Z. X. Ji, T. Xia, M. Meng, C. Low-Kam, R. Liu, S. Pokhrel, S. Lin, X. Wang, Y. P. Liao, M. Y. Wang, L. J. Li, R. Rallo, R. Damoiseaux, D. Telesca, L. Mädler, Y. Cohen, J. I. Zink and A. E. Nel, *ACS Nano*, 2012, **6**, 4349–4368.
21 M. Mortimer, K. Kasemets and A. Kahru, *Toxicology*, 2010, **269**, 182–189.
22 K. Midander, P. Cronholm, H. L. Karlsson, K. Elihn, L. Möller, C. Leygraf and I. O. Wallinder, *Small*, 2009, **5**, 389–399.
23 Z. Y. Wang, N. Li, J. Zhao, J. C. White, P. Qu and B. S. Xing, *Chem. Res. Toxicol.*, 2012, **25**, 1512–1521.
24 Y. Li, W. Zhang, J. F. Niu and Y. S. Chen, *ACS Nano*, 2012, **6**, 5164–5173.
25 A. A. Ammann, *J. Mass Spectrom.*, 2007, **42**, 419–427.
26 T. J. Manning and W. R. Grow, *Chem. Educ.*, 1997, **2**, 1–19.
27 M. S. Xu, D. Fujita, S. Kajiwara, T. Minowa, X. L. Li, T. Takemura and N. Hanagata, *Biomaterials*, 2010, **31**, 8022–8031.
28 S. J. Park, Y. C. Park, S. W. Lee, M. S. Jeong, K. N. Yu, H. Jung, J. K. Lee, J. S. Kim and M. H. Cho, *Toxicol. Lett.*, 2011, **207**, 197–203.
29 H. Yin, P. S. Casey, M. J. McCall and M. Fenech, *Langmuir*, 2010, **26**, 15399–15408.
30 S. George, S. Pokhrel, T. Xia, B. Gilbert, Z. X. Ji, M. Schowalter, A. Rosenauer, R. Damoiseaux, K. A. Bradley, L. Mädler and A. E. Nel, *ACS Nano*, 2010, **4**, 15–29.
31 W. S. Cho, R. Duffin, S. E. M. Howie, C. J. Scotton, W. A. H. Wallace, W. MacNee, M. Bradley, I. L. Megson and K. Donaldson, *Part. Fibre Toxicol.*, 2011, **8**, 27.
32 S. Kittler, C. Greulich, J. Diendorf, M. Koller and M. Epple, *Chem. Mater.*, 2010, **22**, 4548–4554.
33 M. Koch, S. Kiefer, C. Cavelius and A. Kraegeloh, *J. Nanopart. Res.*, 2012, **14**, 646.
34 T. Buerki-Thurnherr, L. S. Xiao, L. Diener, O. Arslan, C. Hirsch, X. Maeder-Althaus, K. Grieder, B. Wampfler, S. Mathur, P. Wick and H. F. Krug, *Nanotoxicology*, 2012, 1–15.
35 C. D. Vecitis, K. R. Zodrow, S. Kang and M. Elimelech, *ACS Nano*, 2010, **4**, 5471–5479.
36 E. Burello and A. P. Worth, *Nanotoxicology*, 2011, **5**, 228–235.

REVIEW

Biological Interpretation of the *In Vitro* Assessment of Nanotoxicity

Nobutaka HANAGATA[1, 2]

[1]*Nanotechnology Innovation Station, National Institute for Materials Science, Tsukuba, Japan*
[2]*Graduate School of Life Science, Hokkaido University, Sapporo, Japan*

Synopsis
Even though nanomaterials are used as constituents of many manufactured articles, there are no unified criteria for evaluating their safety or toxicity. Even the same nanomaterial can cause different sensitivities in different cell types. In addition, differences in physiological conditions can cause varied sensitivity of the same cell type to a specific nanomaterial. Generally, nanomaterials form aggregates or agglomerates in the culture medium, resulting in a range of size variations. Therefore, the response of each cell differs depending on the amount of nanomaterial it absorbs. Furthermore, it is also necessary to consider the effects when a nanomaterial releases metal ions. The most complicated scenario for the *in vitro* evaluation of a nanomaterial is that it affects growth, apoptosis and necrosis collectively. Nanomaterial toxicity arises from generation of reactive oxygen species (ROS) inside the cell. However, many types of cells possess ROS elimination systems. In cells that have the ability to completely remove ROS, cytotoxicity is normally not observed even after exposure to a toxic nanomaterial. However, for cells that are not able to cope with ROS, cytotoxicity occurs. A number of factors determine which specific molecular species of intracellular ROS quenchers or scavengers act inside cells, including cell type, cellular physiological state and the type and amount of nanomaterial present. In this review, we discuss the biological interpretation of nanomaterial toxicity evaluation data.

Key words: *nanotoxicity, assessment, released ions, reactive oxygen species*

Introduction

Nanotechnology has become an essential underlying technology in the generation of new information and communications, the environment, energy and medical industries. In particular, nanomaterials, which are produced by nanotechnology and possess novel features that are not displayed by conventional bulk materials, are currently utilized in the production of widely available nano-derived products such as sporting goods, tires, anti-bacterial fabrics, anti-UV products, cosmetics, electronic appliances, and others. In addition, extensive research has been carried out towards the utilization of nanomaterials for biomedical applications such as diagnosis, imaging, drug delivery, and others, with many products already being used in clinical applications or in the pre-clinical stage of development [1]. Due to their wide-ranging applications, nanomaterials are expected to be used more widely in the future. It is noteworthy, however, that the novelty of nanomaterials also contributes to their unidentified effects to human health and the environment. The impact of nanomaterials on human health is not fully understood. In many cases, therefore, safety concerns outweigh the benefits of nanotechnology [2-7], which has resulted in a slowdown in the use of nanotechnology for industrial applications.

Currently, because there are no formal guidelines for the evaluation of safety and toxicity of nanomaterials, each researcher or manufacturer performs such evaluations by employing diverse methods. This has resulted, for example, in differing results that have been reported on the nanomaterial toxicity of carbon nanotubes (CNTs) or TiO_2 nanoparticles [8-12]. Although it is believed that these differences are mainly caused by insufficient characterization of the physicochemical properties of the nanomaterials, differences in evaluation method and interpretation of results may also give rise to such variation. In this review, we describe the biological interpretation and problems related to nanomaterial toxicity evaluation based on cell activity or viability, and ROS as the main cause of toxicity.

Cytotoxicity Evaluation Method

The cytotoxicity evaluation method can be divided into measurements of the activity of certain cellular enzymes and of dead cells. For the former measure, the 3-(4,5-dimetylthial-2-yl)-2, 5-diphenyltetrazolium bromide (MTT) assay is the most widely used. The MTT assay is based on the correlation between the number of viable cells and the level of formazan dye that is produced by degradation of tetrazolium salt via succinate-tetrazolium reductase that is present in the mitochondrial respiratory chain [13-15]. However, in the presence of toxic materials, the value obtained by the MTT assay does not necessarily correlate with the number of viable cells. When the amount of formazan formed in the MTT assay in the presence of a toxic material is reduced by 50% compared to control cells, the succinate-tetrazolium reductase activity of the entire cell population is reduced by 50% on average. It is not known whether the actual number of living cells is also reduced by 50% or not. Generally, the value obtained from enzyme activity measurements such as the MTT assay is expressed as cell viability. On the other hand, the trypan blue [16], propidium iodide (PI) staining [17-20], EthD-1 staining and lactate dehydrogenase (LDH) activity assay [21, 22] methods evaluate cytotoxicity by detecting or measuring non-living cells. Trypan blue, propidium iodide and EthD-1 are assay methods that utilize the incorporation of dyes into cells, which is facilitated by cell membrane damage. Because the values obtained by these methods correlate with the number of non-viable cells, it is possible to determine the ratio between the number of viable and non-viable cells. Although mitochondrial damage can reduce the amount of formazan produced, if the cells are viable, then the ratio of the number of viable to non-viable cells will be greater than the relative value of cell viability.

Interpretation of toxicity evaluation

The evaluation of cytotoxicity involves many complex factors. As an example, when comparing cultured cells exposed to a toxic material for a certain period of time with an unexposed control, one may observe a 50% reduction in the number of viable cells in the exposed group, but there are several possible ways to interpret this result. First, the toxic material may not have induced cell death but rather slowed down cell proliferation (growth inhibition). Second, the toxic material may have caused the death of 50% of the cell population. And third, the toxic material may have induced both cell death and growth inhibition.

Theoretically, when cell exposure to a toxic material is uniform, just as with water, and the physiological state of all cells is the same, each cell should generate the same response. Therefore, a 50% reduction in the number of viable cells in the presence of a water-soluble toxic material should be interpreted as a 50% average reduction in growth rate. This interpretation is possible if the toxic nanomaterial is uniformly dispersed in the culture medium as a water-soluble substance and behaves uniformly in all cells.

In the case of a toxic material that behaves uniformly in all cells, the next item to consider is what meaning, for example, a 50% reduction in the number of viable cells carries. This number depends on the cultivation time in the presence of the toxic material. For example, cells seeded in the absence of a toxic material at an initial density of 5,000 cells/cm^2 may expand to 20,000 and 80,000 cells/cm^2 in 24 and 48 hours, respectively (with a doubling time in this culture condition of 12 hours), but may reach only 10,000 and 20,000 cells/cm^2, respectively, in the presence of the toxic material due to a growth

inhibition effect (with a doubling time of 24 hours). In this case, viable cell count was reduced by 50% and 75% at the 24-hour and 48-hour incubation period, respectively. In other words, the degree of toxicity changes with the incubation time. This phenomenon is not caused by an increase in toxicity over time but rather because the doubling time became two times slower in the presence of the toxic material. The correct interpretation should be that the toxic material lowered the cell growth rate by 50%. With this interpretation, the level of toxicity remains constant and does not change with time.

As described above, theoretically, all cells are uniformly affected in the case of a toxic material that is water-soluble or homogenously dispersed. However, many nanomaterials form aggregates or agglomerates of various sizes in the culture medium. This means that although a material's primary size may be uniform, its hydrodynamic size may not be (Figure 1). Cells that absorb large sized aggregates and those that absorb small size aggregates retain different intracellular levels of the nanomaterials, which can cause differences in cellular response. Because cells die after absorbing high levels of nanomaterials, while those that absorb low levels survive, the growth rate of an exposed culture will appear to be lower. When the number of viable cells is reduced by 50% due to nanomaterial toxicity, the cause may stem from two factors: cell death or a decrease in growth rate.

Furthermore, nanomaterial-induced cell death can be caused either by apoptosis or necrosis. Apoptosis is programmed cell death that follows the activation of certain signal transduction pathways, and can be considered as a reaction that occurs when a cell determines that it is not able to cope with the toxicity of a nanomaterial. In other words, the cell determines that death is more advantageous than survival. In contrast, necrosis is unregulated cell death caused by damage to various cellular functions by the nanomaterial, leading to a state where metabolic activity drops to zero. Thus, nanomaterials that are not homogenous in the culture medium can impact cells in three complex ways: growth inhibition, apoptosis and necrosis.

Hanagata *et al.* [23] reported that copper oxide nanoparticles (CuO NPs) can cause growth inhibition, apoptosis and necrosis of A549 human lung epithelial cells. In this study,

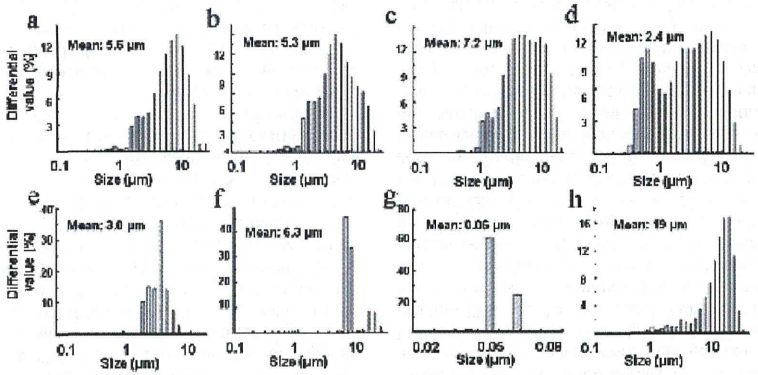

Figure 1 Hydrodynamic size distribution of nano-oxides in cell culture medium with concentration of ~ 50 μg/mL. **(a)** ZnO (~ 60 nm) NPs. **(b)** ZnO (~20 nm) NPs. **(c)** Al-doped ZnO (~ 50 nm) NPs. **(d)** CeO (~ 20 nm) NPs. **(e)** Porous SiO_2 (~ 60 nm). **(f)** non-porous SiO_2 (~ 15 nm). **(g)** Al_2O_3 (~ 15 nm) NPs. **(h)** Al_2O_3 NW. **(i)** CuO NPs. **(j)** Al-doped CuO NPs. The nano-oxides exhibited large size distribution in the cell culture medium and the mean size is much larger than the primary size measured in dry condition.

CuO NPs with an average size of 50 nm added to the culture medium at a concentration of 25μg/mL formed aggregates with an average hydrodynamic size of 300 nm. After culturing for 48 hours followed by exposure to 25μg/mL CuO NPs for 24-hours, viable cell count dropped to 34% of the control level. This reduction was found to be caused by a combination of growth arrest, apoptosis and necrosis [23]. About 18% of the cell population that was exposed to the CuO NPs had experienced cell death, with apoptosis and necrosis accounting for 9% each (Figure 2). Most of the other cells had arrested in the G1 or G2 phase of the cell cycle. After separating viable and non-viable cells followed by transmission electron microscope (TEM) observation of the CuO NPs absorbed by the cells, results clearly showed a higher level of CuO NPs in the non-viable cells vs. viable cells (Figure 3), indicating that the amount of absorbed nanomaterial is one of the factors that determines cellular fate.

Evaluation on the effect of metal ion release

Nanomaterial toxicity measurements become complex when the materials contain metal ions such as Zn, Cu or Ag due to the release by these metal or metal-oxide nanomaterials of metal ions into the medium. It has been reported that the release of metal ions from nanomaterials containing Zn, Cu or Ag to the medium occurs within as little as a few hours to 24 hours [23, 24]. It is believed that if these nanomaterials are absorbed quickly into the cells, the effects of ion release are minimal. However, cells are normally affected by both the ions released by the nanoparticles prior to their absorption and the absorbed nanoparticles themselves. The cyto-

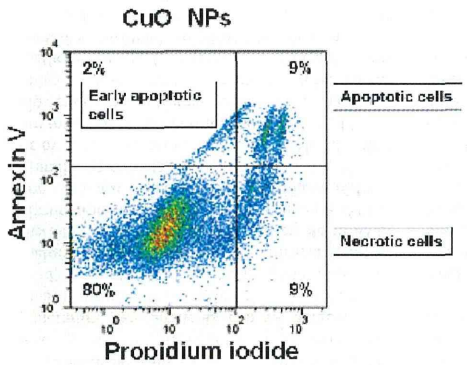

Figure 2 Ratio of dead cells determined by using flow cytometery. Cells were stained by propidium iodide and annexin V labeled with FITC. Apoptoticand necrotic cells were distributed upper right-hand and lower right-hand areas, respectively. Twenty thousand human lung epithelial A549 cells that were exposed to 25 μg/mL CuO NPs were analyzed.

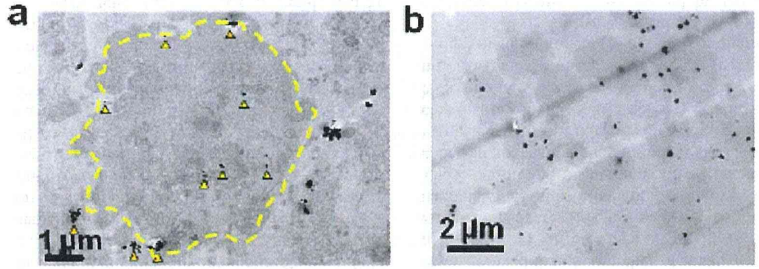

Figure 3 Internalized CuO NPs observed by transmission electron microscope. **(a)** Internalized CuO NPs (arrowhead) in living A549 cell. Dotted line indicates outline of cell. **(b)** Internalized CuO NPs in dead cell. Dead cell detached from culture tissue were observed.

toxicity of silver nanoparticles (Ag NPs) was mainly caused by Ag ions released into the medium [25]. In contrast, the toxicity of CuO NPs due to released ions was not as significant [24, 26]. Hanagata *et al.* [23] investigated the effects of Cu ions released from CuO NPs on A549 cells. CuO NPs at a concentration of 25μg/mL were added to Dulbecco modified Eagle's medium (DMEM), followed by incubation of the cells at 37°C. After 24 hours, the culture was centrifuged at 150,000 g for 60 mins and the Cu concentration in the supernatant was determined as 13μg/mL. CuO NPs were not detected when the supernatant was analyzed by a laser diffraction particle size analyzer (LDS). Further observation of the supernatant using transmission electron microscopy (TEM) and energy dispersive spectroscopy (EDS) also confirmed the absence of CuO NPs. The measured Cu present in the supernatant was therefore composed of Cu ions that had been released from the CuO NPs. Cells grown in this supernatant for 24 hours had a viable cell count of about 80% of control. Because cells grown in a medium containing 25μg/ml CuO NPs for 24 hours had a viable cell count of about 35% of control, it was estimated that the Cu ions that were released from CuO-NPs contributed a maximum of 30% towards the toxicity of CuO-NPs (= (100-80)/(100-35)). Regarding the toxicity of ZnO NPs, there are conflicting reports on the effect of Zn ions released into the culture medium. Deng *et al.* [27] reported a profound effect, whereas Lin *et al.* [28] did not. Sasidharan *et al.* [29] showed that the amount of Zn ions released from ZnO NPs depends on the pH of the medium. The release of Zn ions at pH 5.0 was significantly higher than at pH 7.0. Thus, the release of Zn ions from ZnO NPs is affected by the extracellular environment, and the amount of released Zn ions further contributes to the toxicity of ZnO NPs

Nanomaterial toxicity and reactive oxygen species generation

Much research has shown that ROS are the main contributor to the toxicity of nanomaterials that are absorbed into the cell. In addition, for CuO NPs and ZnO NPs, the released ions can also generate ROS. Therefore, ROS generation itself can likely be used as an indication of nanomaterial toxicity.

The mechanism of ROS generation by nanomaterials absorbed intracellularly differs according to the chemical composition of the nanomaterials. For nanomaterials that contain transition metals such as iron, ROS generation has been suggested to occur through the Fenton reaction [30]. On the other hand, ROS generation by ZnO NPs was proposed to occur at the surface of the ZnO NPs as a result of continuous oxidation-reduction reactions caused by amino acid-Zn^{2+}/Zn^{+} redox properties, e.g., glycine-Zn^{2+}/Zn^{+} [28, 31]. Xia *et al.* [32] showed that ROS generation by ZnO NPs occurs in endosomes. Furthermore, ROS generation by nanomaterials has also been shown to arise via the change in mitochondrial function resulting from nanomaterials absorbed by the mitochondria [33, 34]. Also, CNTs absorbed by the cell have been reported to cause ROS generation [35-37], although the mechanism for this is not well understood. A main cause of ROS generation by CNTs was also reported to be impurities from the CNT manufacturing processes [38, 39].

Ostrovsky *et al.* [40] reported the existence of a correlation between nanomaterial toxicity and ROS generation. They found that ZnO NPs are toxic to human glioma cells but not to human astrocytes. Examination of ROS generation using 2,7-diachlorofluorescein diacetate showed that the amount of ROS production increased significantly in glioma cells, but not astrocytes, when cells were exposed to ZnO NPs. Furthermore, the toxicity of ZnO NPs in glioma cells was reduced when ROS generation was inhibited by the antioxidant N-acetyl cysteine (NAC), indicating that ROS generation was the cause of the toxicity. Similarly, exposure of A549 cells to CuO NPs causes ROS generation depending on the concentration of CuO NPs (Figure 4), and CuO NP toxicity was reduced in the presence of NAC [23], indicating that CuO NP toxicity is caused by ROS generation. Furthermore, Hanley *et al.* [41] reported that ZnO NPs were non-toxic to human lymphocytes but were toxic to monocytes, with the toxicity being caused by the difference in ROS generation levels. In addition, Yang *et al.* [42] proposed that in addition to ROS generation, the toxicity of 20 nm SiO_2 NPs

in RAW264.7 cells was also due to its effect in increasing intracellular Ca^{2+} concentration. Toxicity caused by increased intracellular Ca^{2+} concentration has also been reported in human bronchial epithelial cells (BEAS-2B) exposed to ZnO NPs [43] and Ag NPs [34, 44, 45]. It was suggested that inhibition of ZnO NP toxicity in BEAS-2B cells by the NAC antioxidant was the result of inhibition by NAC of the influx of Ca^{2+} from the extracellular medium to intracellular compartments, indicating that both ROS production and an increase in intracellular Ca^{2+} concentration are involved in toxicity.

ROS generation by toxic materials can be determined not only by direct quantification but also by indirect measurements. Indirect ROS generation measurements can be achieved by quantification of molecules that are related to oxidative stress such as glutathione or malondialdehyde [46-48], or by measurement of the activity of enzymes that participate in ROS elimination such as superoxide dismutase (SOD) and catalase, glutathione peroxidase (GPX), glutathione reductase, and others [46, 47, 49, 50], or by gene expression analysis of molecules that are involved in ROS elimination [23, 25, 43, 51]. However, two different results have been obtained using these respective measurement methods. In the first result, the molecules and enzymes involved in ROS elimination were damaged by the nanomaterial, which caused an increase in intracellular oxidative stress [47, 48, 50, 52]. The increase in oxidative stress led to an increase in lipid peroxidation [28, 47, 52] that further led to genotoxicity [47, 50]. The other result showed that the number of molecules and the activation of enzymes involved in ROS elimination increased in the presence of the nanomaterials, thus alleviating oxidative stress. These conflicting results may arise from differences in the nanomaterial toxicity level. Cells incubated with metal or metal oxide nanoparticles that are highly toxic such as Ag NPs, CuO NPs, or ZnO NPs were reported to effect a significant increase in the expression of genes encoding metallothionein (MT) family proteins [23, 25, 51]. MT is known as a molecule that can overcome oxidative stress caused by the presence of excess metal ions [53-60]. Therefore, an increase in the expression of MT family genes in response to Ag NPs, CuO NPs, or ZnO NPs is involved in ROS elimination. On the other hand, ZnO NPs were reported to reduce the amount of glutathione and the activities of enzymes involved in ROS elimination such as catalase and SOD [47]. Because the hydroxyl radical scavenging activity of MT is more than 300 times higher than glutathione [61], it is likely that the MT family proteins are the main factor in the cellular response to ROS generation in the presence of ZnO NPs. In other words, although the level of glutathione and the activities of catalase and/or SOD are reduced by ZnO NPs, cells can alleviate ROS toxicity via MT family proteins. When evaluating nanomaterial toxicity by quantitative measurements of molecules that are related to oxidative stress such as glutathione and malondialdehyde; by the activity of enzymes

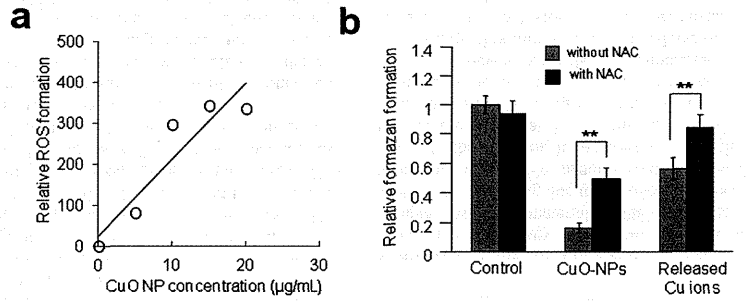

Figure 4 Toxicity of CuO NPs caused by generation of reactive oxygen species (ROS). **(a)** Relationship between CuO NP concentration and intracellular ROS generation. **(b)** NAC treatment reduces the toxicity of CuO NPs because of antioxidant action of NAC.

that participate in ROS elimination such as SOD, catalase, GPX and glutathione reductase; or by expression analysis of the genes involved in ROS elimination, it is important to assess whether or not the measured molecule(s) or enzyme(s) play a central role in the ROS pathway.

Generation of ROS by nanomaterials was reported to increase the activation of p53 and the Bax/Bcl-2 ratio, and induce the expression of apoptosis-related genes, ultimately leading to apoptosis [43, 62]. Apoptosis induction by ROS may also be explained by the fact that overexpression of MT that participates in ROS elimination can prevent cells from entering the apoptotic pathway [63]. In addition, oxidative stress due to ROS induces the inflammatory response [64, 65]. In many cases, ROS are the cause of DNA damage [66-73]. Furthermore, it has been reported that oxidative stress caused by nanoparticles induces the formation of the guanine adduct 8-hydroxy deoxyguanisine (8-OH-dG), which has been suggested to have an important role in carcinogenesis [74, 75].

The relationship between ROS generation caused by nanomaterials absorption and toxicity can be explained by the model shown in Figure 5. If the level of ROS generation by nanomaterials is low, cells can completely remove ROS by using their naturally induced ROS elimination systems. In such a case, no apparent toxicity ensues. However, if the level of ROS generation by nanomaterials cannot be overcome by the naturally induced ROS elimination systems, remaining ROS are able to cause cytotoxicity. Differences in the toxicity of the same nanomaterials in different cell types may be caused by differences in ROS elimination systems that each cell type possesses. When the amount of remaining ROS is low, cells experience growth inhibition, and when the amount of remaining ROS is high, cell death ensues. As cell death can either be apoptotic or necrotic in nature, which pathway the cell ultimately takes may depend on the remaining ROS.

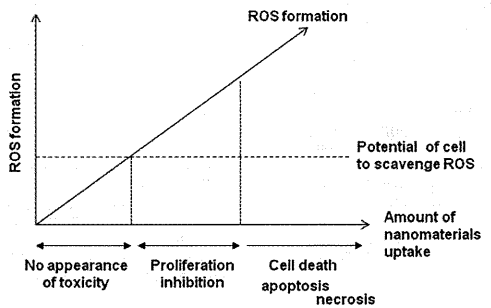

Figure 5 Proposed model for the relationship between ROS generation and toxicity.

Conclusions

So far, much research on the toxicity and safety of nanomaterials has been performed. Although many review articles describing the degree and mechanism of action of various nanomaterials have been published, much less attention has been paid to the interpretation of toxicity evaluation results. Evaluation of nanomaterial toxicity by the MTT assay cannot differentiate whether a decrease in cell viability is caused by a decrease in growth rate or by cell death. It has been reported that in many cases, nanomaterial toxicity is caused by ROS. However, because cells possess ROS elimination systems, the amount of ROS generation measured in assays reflects the amount of ROS that cannot be removed by such systems. Cells possess various ROS elimination systems and information detailing which systems primarily work for different nanomaterials is lacking. In order to generalize information concerning the toxicity of a particular nanomaterial in a certain cell type under certain conditions, careful biological interpretation of toxicity data is important.

References

1) Dobrovolskaia MA, McNeil S. Immunological properties of engineered nanomaterials. Nature Nanotechnology 2007; 2: 469-478.
2) Brumfiel G. Nanotechnology: A little knowledge. Nature 2003; 424: 246-248.
3) Dreher KL. Health and environmental impact of nanotechnology: Toxicological assessment of manufactured nanoparticles. Toxicol Sci 2004; 77: 3-5.
4) Giles J. Nanotechnology: What is there to fear from something so small? Nature 2003; 426: 750
5) Hood E. Nanotechnology: Looking as we leap. Environ. Health Perspect 2004; 112: A740-A749
6) Maynard AD, Kuempel E. Airborne nanostructured particles and occupational health. J Nanopart Res 2005; 7: 587-614.
7) Seaton A, Donaldson K. Nanoscience, nanotoxicology, and the need to think small. Lancet 2005; 365: 923-924.
8) Aillon KL, Xie Y, El-Gendy N, Berkland CJ, Forrest ML. Effects of nanomaterial physicochemical properties on in vivo toxicity. Adv Drug Deliv Rev 2009; 61: 457-466.
9) Jia G, Wang HF, Yan L, Wang X, Pei R, Yan T, Zhao Y, Guo X. Cytotoxicity of carbon nanomaterials: single-wall nanotube, multi-wall nanotube, and fullerene. Environ Sci Technol 2005; 39: 1378-1383.
10) Isobe H, Tanaka T, Maeda R, Noiri E, Solin N, Yudasaka M, Iijima S, Nakamura E. Preparation, purification, characterization, and cytotoxicity assessment of water-soluble, transition-metal-free carbon nanotube aggregates. Angew Chem Int Ed 2006; 45: 6676-6680.
11) Johnston HJ, Hutchinson GR, Christensen FM, Peters S, Hankin S, Srone V. Identification of the mechanisms that drive the toxicity of TiO2 particles: the contribution of phycochemical characteristics. Part Fibre Toxicol 2009; 6: 1-33.
12) Braydich-Stolle LK, Schaeubin NM, Murdock RC, Jiang J, Biswas P, Schlager JJ, Hussain SM. Crystal structure mediates mode of cell death in TiO2 nanotoxicity. J Nanopart Res 2009; 11: 1361-1374.
13) Mosmann T. Rapid colorimetric assay for cellular growth and survival: Application to proliferation and cytotoxicity assays. J Immunol Methods 1983; 65: 55-63.
14) Liu Y, Peterson DA, Kimura H, Schubert D. Mechanism of cellular 3-(4,5-Dimethyl-2-thiazolyl)-2,5-diphenyl-2H tetrazolium bromide (MTT) reduction. J Neurochem 1997; 69, 581-593.
15) Pereira C, Oliveira CR. Oxidative glutamate toxicity involves mitochondrial dysfunction and perturbation of intracellular Ca2+ homeostasis. Neurosci Res 2000; 37: 227-236.
16) Jones KH, Senft JA. An Improved Method to Determine Cell Viability by Simultaneous Staining with Fluorescein Diacetate-Propidium Iodide, J Histochem Cytochem 1985; 33, 77-79.
17) Taylor IW, Milthorpe BK. An Evaluation of DNA Fluochromes, Staining Techniques, and Analysis for Flow Cytometry. I. Unperturebed Cellpopulations. J Histochem Cytochem 1980; 28: 1224-1232.
18) Vuist WMJ, Buitenen FV, De Rie MA, Hekman A, Ruemke P, Melief CJM. Potentiation by Interleukin 2 of Burkitt's Lymphoma Therapy with Anti-Pan B (Anti-CD19) Monoclonal Antibodies in a Mouse Xenotransplantation Model. Cancer Res 1989; 49: 3783-3788.
19) El-Naggar AK, Batsakis JG, Teague K, Garnsey L, Barlogie B. Single- and Double-stranded RNA Measurements by Flow Cytometry in Solid Neoplasms. Cytometry 1991; 12: 330-335.
20) Souchier C, Ffrench M, Benchaib M, Catallo R, Bryon PA. Methods for Cell Proliferation Analysis by Fluorescent Image Cytometry. Cytometry 1995; 20: 203-209.
21) Korzeniewski C, Callewaert DM. An enzyme-release assay for natural cytotoxicity. J Immunol Meth 1983; 64: 313-20.
22) Decker T, Lohmann-Matthes ML. (1988) A quick and simple method for the quantitation of lactate dehydrogenase release in measurements of cellular cytotoxicity and tumor necrosis factor (TNF) activity. J Immunol Meth 1988; 115: 61-9.
23) Hanagata N, Zhuang F, Connolly S, Li J, Ogawa N, Xu M. Molecular response to CuO nanoparticle toxicity in human lung epithelial cells. ACS Nano 5:9326-9338 (2011)
24) Midander K, Cronholm P, Karlsson HL, Elihn K, Moeller L, Leygraf C, Wallinder IO. Surface characteristics, copper release, and toxicity of nano- and micrometer-sized copper and copper(II) oxide particles: A cross-disciplinary study. Small 2009; 5: 389-399.
25) Xu L, Takemura T, Xu M, Hanagata N. Toxicity of silver nanoparticles as assessed by global gene expression analysis. Mater Expr 2011; 1: 74-79.
26) Karlsson HL, Cronholm P, Gustafsson J, Moeller L. Copper oxide nanoparticles are highly toxic: A comparison between metal oxide nanoparticles and carbon nanotubes. Chem Res Toxicol 2008; 21: 1726-1732.
27) Deng X, Luan Q, Chen W, Wang Y, Wu M, Zhang H, Jiao Z. Nanosized zinc oxide particles induce neural stem cell apoptosis. Nanotechnology 2009; 20: 115101(7pp)
28) Lin W, Xu Y, Huang C-C, Ma Y, Shannon KB, Chen D-R, Huang Y-W. Toxicity of nano- and micro-sized ZnO particles in human lung

epithelial cells. J Nanopart Res 2009; 11: 25-39.
29) Sasidharan A, Chandran P, Menon D, Raman S, Nair S, Koyakutty M. Rapid dissolution of ZnO nanocrystals in acidic cancer microenvironment leading to preferential apoptosis. Nanoscale 3:3657-3669 (2011)
30) Risom L, Moller P, Loft S. Oxidative stress-induced DNA damage by particular air pollution. Mutat Res 2005; 592: 119-137.
31) Ai H, Bu Y, Han K. Glycine-Zn+/Zn2+ and their hydrates: on the number of water molecules necessary to stabilize the zwitterionic glycine-Zn+/Zn2+ over the nonzwitterionic ones. J Chem Phys 2003; 118: 10973-10985.
32) Xia T, Kovochich M, Liong M, Madler L, Gilbert B, Shi H, Yeh JI, Zink JI, Nel AE. Comparison of the mechanism of toxicity of zinc oxide and cerium oxide nanoparticles based on dissolution and oxidative stress properties. ACS Nano 2008; 2: 2121-2134.
33) Li N, Sioutas C, Cho A, Schmitz D, Misra C, Sempf J, Wang M, Oberley T, Froines J, Nel A. Ultrafine particle pollutants induce oxidative stress and mitochondrial damage. Environ Health Perspect 2003; 111: 455-460.
34) AshaRani PV, Low Kah MG, Hande MP, Valiyaveettil S. Cytotoxicity and genotoxicity of silver nanoparticles in human cells. ACS Nano 2009b; 3: 279-290.
35) Shvedova AA, Kagan VE. The role of nanotoxicology in realizing the 'helping without harm' paradigm of nanomedicine: lessons from studies of pulmonary effects of single-walled carbon nanotubes. J Internal Med 2010; 267: 106-118.
36) Johnston HJ, Hutchison GR, Christensen FM, Peters S, Hankin S, Aschberger K, Stone V. A critical review of the biological mechanisms underlaying the in vivo and in vitro toxicity of carbon nanotubes: The contribution of physic-chemical characteristics. Nanotoxicology 2010; 4: 207-246.
37) Hu XK, Cook S, Wang P, Hwang HM, Liu X, Williams QL. In vitro evaluation of cytotoxicity of engineered carbon nanotubes in selected human cell lines. Sci Total Environ 2010; 408: 1812-1817.
38) Pulskamp K, Diabate S, Krug HF. Carbon nanotubes show no sign of acute toxicity but induce intracellular reactive oxygen species in dependence on contaminats. Toxicol Lett. 2007, 168:58-74.
39) Vittorio O, Raffa V, Cuschieri A. Influence of purity and surface oxidation on cytotoxicity of multiwalled carbon nanotubes with human neuroblastma cells. Nanomedicine: NBM 2009; 5: 424-431.
40) Ostrovsky S, Kazimirsky G, Gedanken A, Brodie C. Selective cytotoxic effect of ZnO nanoparticles on glioma cells. Nano Res 2009; 2:882-890.
41) Hanley C, Thurber A, Hanna C, Punnoose A, Zhang JH, Winngett DG. The influences of cell type and ZnO nanoparticles size on immune cell cytotoxicity and cytokine induction. Nanoscale Res Lett 2009; 4: 1409-1420.
42) Yang H, Wu QY, Tang M, Kong L, Lu ZH. Cell membrane injury induced by silica nanoparticles in mouse macrophage. J Biomed Nanotech 2009a; 5: 528-535.
43) Huang CC, Aronstam RS, Chen DR, Huang YW. Oxidative stress, calcium homeostasis, and altered gene expression in human lung epithelial cells exposed to ZnO nanoparticles. Toxicol In Vitro 2010; 24: 45-55.
44) AshaRani PV, Hande MP, Valiyaveettil S. Anti-proliferative activity of silver nanoparticles. BMC Cell Biol. 2009; 10: 65.
45) Moutin MJ, Abramson JJ, Salama G, Dupont Y. Rapid Ag+-induced release of Ca2+ from sarcoplasmic reticulum vesicles of skeletal muscle: a rapid filtration study. Biochem Biophys Acta 1989; 984: 289-292.
46) Yang H, Liu C, Yang DF, Zhang HS, Xi ZG. Comparative study of cytotoxicity, oxidative stress and genotoxicity induced by four typical nanomaterials: the role of particle size, shape and composition. J Appl Toxicol 2009b; 29: 69-78.
47) Sharma V, Shukla RK, Saxena N, Parmar D, Das M, Dhawan A. DNA damaging potential of zinc oxide nanopaticles in human epidermal cells. Toxicol Lett 2009; 185: 211-218.
48) Gerloff K, Albrecht C, Boots AW, Forster I, Schins RPF. Cytotoxicity and oxidative DNA damage by nanoparticles in human intestinal CaCo-2 cells. Nanotoxicology 2009; 3: 255-264.
49) Fahmy B, Cormier SA. Copper oxide nanoparticles induce oxidative stress and cytotoxicity in airway epithelial cells. Toxicol In Vitro 2009; 23: 1365-1371.
50) Alarifi S., Ali D., Alkahtani., Verma A., Ahamed M., Ahmed M., Alhadlaq HA. Induction of oxidative stress, DNA damage, and apoptosis in a malignant human skin melanoma cell line after exposure to zinc oxide nanoparticles. Int. J. Nanomed. 8: 983-993 (2013)
51) Hanagata N, Xu M,Takemura T, Zhuang F. Cellular responses to ZnO nanoparticles inferred from global gene expression analysis. Nano Biomed 2010; 2: 153-169.
52) Wang F, Gao F, Lan MB, Yuan HH, Huang YP, Liu JW. Oxidative stress contributes to silica nanoparticle-induced cytotoxicity in human embryonic kidney cells. Toxicol In Vitro2009; 23: 808-815.

53) Andrews GK. Regulation of metallothionein gene expression by oxidative stress and metal ions. Biochem Pharmacol 2000; 59: 95-104.
54) Huang Y-C T, Li Z, Carter JD, Soukup JM, Schwartz DA, Yang IV. Fine ambient particles induce oxidative stress and metal binding genes in human alveolar macrophages. Am J Respir Cell Mol Biol 2009; 41: 544-552.
55) Min KS, Morishita F, Tetsuchikawahara N, and Onosaka S. Induction of hepatic and renal metallothionein synthesis by ferric nitrilotriacetate in mice: the role of MT as an antioxidant. Toxicol Appl Pharmacol 2005; 204: 9–17.
56) Kumai MVR, Hiramatsu M, Ebadi M. Free radical scavenging actions of metallothionein isoforms I and II. Free Rad Res 1998;29:93-101.
57) Sato M, Kondoh M. Recent studies on metallothionein: protection agaist toxicity of heavy metals and oxygen free radicals. The Tohoku J Exp Med 2002; 196: 9-22.
58) Bauman JW, Madhu C, McKim Jr JM, Liu Y, Klaassen CD. Induction of hepatic metallothionein by paraquat. Toxicol Appl Pharmacol 1992; 117: 233-241.
59) Dalton T, Palmiter RD, Andrews GK. Transcriptional induction of the mouse metallothionein-I gene in hydrogen peroxide-treated Hepa cells involves a composite major late transcription factor/antioxidant response element and metal response promoter elements. Nucleic Acid Res 1994; 22: 5016-5023.
60) Thornalley PJ, Vasak M. Possible role for metallothionein in protection against radiation-induced oxidative stress. Kinetics and mechanism of its reaction with superoxide and hydroxyl radicals. Biochim Biophys Acta 1985; 827: 36-44.
61) Vliagoftis H, Schwingshackl A, Milne CD, Duszyk M, Hollenberg MD, Wallace JL, Befus AD, Moqbel R. Proteinase-activated receptor-2-mediated matrix metalloproteinase-9 release from airway epithelial cells. J Allergy Clinic Immunol 2000; 106: 537-545.
62) Ye YY, Liu JW, Xu JH, Sun LJ, Chen MC, Lan MB. Nano-SiO2 induces apoptosis via activation of p53 and Bax mediated by oxidative stress in human hepatic cell line. Toxicol In Vitro 2010; 24: 751-758.
63) Jayasurya A, Bay BH, Yap WM, Tan NG. Correlation of metallothionein expression with apoptosis in nasapharyngeal carcinoma. Brit J Cancer 2000; 82: 1198–1203.
64) Donaldson K, Tran CL. Inflammation caused by particles and fibers. Inhal Toxicol 2002; 14: 5-27.
65) Donaldeson K, Tran L, Jimenez LA, Duffin R, Newby DE, Mills N, MacNee W, Stone V. Comburstion-derived nanoparticles: A review of their toxicology following inhalation exposure. Part Fibre Toxicol 2005; 2: 10.
66) Wu WS, Tsai RK, Chang CH, Wang S, Wu JR, Chang YX. Reactive oxygen species mediated sustained activation of protein kinase C and ERK for migration of human hepatoma cell HepG2. Mol Cancer Res 2006; 4:747-58.
67) Valko M, Rhodes CJ, Moncol J, Izakovic M, Mazur M. Free radicals, metals and antioxidants in oxidative stress induced cancer. Chem Biol Interact 2006; 160:1-40.
68) Hussain SM, Hess KL, Gearhart JM, Geiss KT, Schlager JJ. In vitro toxicity of nanoparticles in BRL 3A rat liver cells. Toxicol In Vitro 2005; 19:975-83.
69) Carlson C, Hussain SM, Schrand AM, Braydich-Stolle LK, Hess KL, Jones RL, Schlager JJ. Unique cellular interaction of silver nanoparticles: size-dependent generation of reactive oxygen species. J Phys Chem 2008; 112:13608-19.
70) Hsin, YH, Chen CF, Huang S, Shih TS, Lai PS, Chueh PJ. The apoptosis effect of nanosilver is mediated by a ROS- and JNK-dependent mechanism involving the mitochondrial pathway in NIH3T3 cells. Toxicol Lett 2008; 197:130-9.
71) Xia T, Kovochich M, Brant J, Hotze M, Sempf J, Oberley T, Sioutas C, Yeh JI, Wiesner MR, Nel AE. Comparison of the abilities of ambient and manufactured nanoparticles ti induce cellular toxicity according to an oxidative stress paradigm. Nano Lett 2006; 6:1794-807.
72) Foldbjerg R, Dang DA, Autrup H. Cytotoxicity and genotoxicity of silver nanoparticles in the human lung cancer cell line, A549. Arch Toxicol. 2011, 85:743-50.
73) Beru Be K, Balharry D, Sexton K, Koshy L, Jones T. Combustion-derived nanoparticles: Mechanisms of pulmonary toxicity. Clin Exp Pharmacol Physiol 2007; 34: 1044-1050.
74) Schins RP. Mechanisms of genotoxicity of particles and fibers. Inhal Toxicol 2002; 14: 57-78.
75) Schins RP, Knappen AM, Cakmak GD, Shi T, Weishaupt C, Borm PJ. Oxidant-induced DNA damage by quartz in alveolar epithelial cells. Mutat Res 2002; 517: 77-86.

(Received: May 31, 2013/
Accepted: June 23, 2013)

Corresponding author:
Prof. Nobutaka Hanagata
Nanotechnology Innovation Station,
National Institute for Materials Science
1-2-1 Sengen, Tsukuba, Ibaraki 305-0047, Japan
Tel: +81-29-860-4774
Fax: +81-29-859-2475
E-mail: HANAGATA.Nobutaka@nims.go.jp

OPEN ACCESS
IOP PUBLISHING
SCIENCE AND TECHNOLOGY OF ADVANCED MATERIALS
Sci. Technol. Adv. Mater. **14** (2013) 055009 (10pp)
doi:10.1088/1468-6996/14/5/055009

Preparation and characterization of multifunctional magnetic mesoporous calcium silicate materials

Jianhua Zhang[1], Yufang Zhu[2], Jie Li[3], Min Zhu[2], Cuilian Tao[1] and Nobutaka Hanagata[3]

[1] School of Medical Instrument and Food Engineering, University of Shanghai for Science and Technology, 516 Jungong Road, Shanghai 200093, People's Republic of China
[2] School of Materials Science and Engineering, University of Shanghai for Science and Technology, 516 Jungong Road, Shanghai 200093, People's Republic of China
[3] Interdisciplinary Laboratory for Nanoscale Science and Technology, National Institute for Materials Science, 1-2-1 Sengen, Tsukuba, Ibaraki 305-0047, Japan

E-mail: zjf2412@163.com

Received 14 July 2013
Accepted for publication 26 September 2013
Published 22 October 2013
Online at stacks.iop.org/STAM/14/055009

Abstract

We have prepared multifunctional magnetic mesoporous Fe–$CaSiO_3$ materials using triblock copolymer (P123) as a structure-directing agent. The effects of Fe substitution on the mesoporous structure, *in vitro* bioactivity, magnetic heating ability and drug delivery property of mesoporous $CaSiO_3$ materials were investigated. Mesoporous Fe–$CaSiO_3$ materials had similar mesoporous channels (5–6 nm) with different Fe substitution. When 5 and 10% Fe were substituted for Ca in mesoporous $CaSiO_3$ materials, mesoporous Fe–$CaSiO_3$ materials still showed good apatite-formation ability and had no cytotoxic effect on osteoblast-like MC3T3-E1 cells evaluated by the elution cell culture assay. On the other hand, mesoporous Fe–$CaSiO_3$ materials could generate heat to raise the temperature of the surrounding environment in an alternating magnetic field due to their superparamagnetic property. When we use gentamicin (GS) as a model drug, mesoporous Fe–$CaSiO_3$ materials release GS in a sustained manner. Therefore, magnetic mesoporous Fe–$CaSiO_3$ materials would be a promising multifunctional platform with bone regeneration, local drug delivery and magnetic hyperthermia.

Keywords: mesoporous calcium silicate, magnetic hyperthermia, drug delivery, bone regeneration

1. Introduction

Calcium silicate ($CaSiO_3$) materials, a classic example of Ca–Si-based bioceramics, have been proposed as potential bioactive materials for bone tissue regeneration due to their excellent bioactivity and degradability [1–4]. Studies demonstrated that biomaterials with high specific surface area and pore volume could accelerate the kinetic process of apatite formation and therefore, enhance the bone-forming bioactivity [5, 6]. In recent years, many efforts have been made to develop mesoporous $CaSiO_3$ materials for bone regeneration [7–12], because mesoporous materials have unique structural characteristics including high specific surface area, large pore volume and controllable porosity at mesoscale [13]. Li *et al* [7] synthesized mesoporous $CaSiO_3$ materials using mesoporous silica SBA-15 as the template and silicon source, which exhibited a significantly enhanced bone-forming ability compared to the conventional amorphous $CaSiO_3$ materials. Chang and co-workers [8, 9] prepared mesoporous $CaSiO_3$ materials using the surfactant templating method to study its potential application in filling the apical root canals of teeth. In addition, Wei *et al* [10] and Zhu *et al* [11] designed mesoporous $CaSiO_3$/polymer composites for potential use in hard tissue repair. On the other hand, mesoporous materials have been considered as promising carriers for drug delivery [13, 14], and mesoporous $CaSiO_3$ nanoparticles could also exhibit sustained drug delivery ability [12]. Therefore, mesoporous $CaSiO_3$ materials with local drug delivery would be beneficial for bone regeneration.

Generally, both texture and composition of bioceramics control their physicochemical and biological properties [15–17]. Studies demonstrated that the incorporation of zinc (Zn), strontium (Sr), titanium (Ti) or magnesium (Mg) in $CaSiO_3$ ceramics improved their physicochemical and biological properties [18–24]. For example, Ramaswamy *et al* [19] incorporated Zn into Ca–Si system to form $Ca_2ZnSi_2O_7$ ceramics, and found that $Ca_2ZnSi_2O_7$ ceramics supported osteoblast-like cells attachment with a well-organized cytoskeleton structure and significantly increased cellular proliferation and differentiation compared to $CaSiO_3$ ceramics. Lu *et al* [23] synthesized a mesoporous magnesium–$CaSiO_3$, which could support cell attachment and promote the proliferation and differentiation of MC3T3-E1 cells. We recently substituted Sr into mesoporous $CaSiO_3$ materials, and found that the mesoporous Sr–$CaSiO_3$ materials kept mesoporous structure and enhanced the proliferation and alkaline phosphatase activity of MC3T3-E1 cells compared to the mesoporous $CaSiO_3$ materials [24].

Iron (Fe) plays a vital role in the functioning of body with Fe pool in humans being found in the red blood cells, with a lesser extent in the tissues and a small amount circulating in the plasma [25]. Studies demonstrated that the Fe-containing bioceramics could stimulate their cell response ability [26–29]. For example, Wu *et al* [26] fabricated a CaP ceramic–magnetite nanoparticles (CaP–MNP) composite, and the *in vitro* results indicated that the CaP–MNP composite was able to significantly promote Ros17/2.8 and MG63 cells' proliferation and differentiation compared to ordinary CaP ceramics. Panseri *et al* developed magnetic hydroxyapatite scaffolds to enhance tissue regeneration. The hydroxyapatite/magnetite 90/10 scaffolds were shown to enhance cell proliferation at the early stage, and a good level of histocompatibility was observed in a critical size lesion of the rabbit condyle *in vivo* [27]. On the other hand, studies demonstrated that magnetic bioceramics could generate heat under alternating magnetic field and be used for hyperthermia therapy in bone defects caused by bone tumors [30–33], because cancer cells generally perish around 43 °C due to hemorrhage, stasis and vascular occlusion, whereas normal cells are not damaged until higher temperature [33, 34].

Therefore, we hypothesized that mesoporous Fe-doped $CaSiO_3$ (Fe–$CaSiO_3$) materials could induce an improved bone-forming bioactivity and stimulate bone cell growth due to the mesoporous structure and the Fe incorporation. Furthermore, mesoporous Fe–$CaSiO_3$ materials could effectively load drugs or growth factors as a potential local drug delivery system, and could be magnetic seeds for magnetic hyperthermia treatment. It can be believed that mesoporous Fe–$CaSiO_3$ materials would be a promising multifunctional platform with bone regeneration, local drug delivery and magnetic hyperthermia for the treatment of bone defects caused by bone tumors after surgery. Recently, magnetic mesoporous iron oxide and silica particles were developed for drug delivery and hyperthermia therapy, but they were not bioactive for bone regeneration [32, 35–37]. We prepared magnetic mesoporous bioactive glass scaffolds, which showed the potential for bone regeneration with bioactivity, sustained drug delivery and magnetic hyperthermia properties [38, 39]. However, the preparation procedure was multistep and rather complex. To the best of our knowledge, there are no previous reports describing the preparation of magnetic mesoporous Fe–$CaSiO_3$ materials and further investigating their multifunctionality for bone regeneration.

In this study, we have successfully prepared magnetic mesoporous Fe–$CaSiO_3$ materials using triblock copolymer (P123) as a structure-directing agent. The effects of the Fe substitution on the mesoporous structure, magnetic heating ability and *in vitro* bioactivity of mesoporous $CaSiO_3$ materials have been investigated. Gentamicin, an antibiotic for treating osteomyelitis, was used as a model drug and introduced into mesoporous Fe–$CaSiO_3$ materials to evaluate the drug delivery property.

2. Experimental methods

2.1. Preparation and characterization of mesoporous Fe–$CaSiO_3$ materials

Mesoporous Fe-–$CaSiO_3$ materials were prepared according to the previously reported method with some modifications [8]. The chemical compositions and the sample names are listed in table 1. In a typical synthesis for mesoporous 5%Fe–$CaSiO_3$ materials, 3.0 g of P123 (Mw = 5800, Aldrich) was dissolved in 130 ml of H_2O and 20.5 ml of HCl (⩾37%, Sigma-Aldrich) while stirring at 38 °C in oil bath until the solution became clear. After the addition and dissolution of 9.15 g of $Ca(NO_3)_2 \cdot 4H_2O$ (Aldrich) and 0.824 g of $Fe(NO_3)_3 \cdot 9H_2O$ (Aldrich) in P123 solution, 8.5 g of tetraethyl orthosilicate (TEOS, 98%, Aldrich) was then added into the solution. The mixture was stirred at 38 °C for 24 h, and the resulting precipitate was dried at 100 C for 24 h in air without any filtering and washing. The as-synthesized materials were calcined from room temperature to 600 °C with a heating rate of 1 °C min^{-1}, and maintained at 600 °C for 6 h to remove the templates. Finally, the calcined materials were treated in 10% H_2 per 90% Ar at 400 °C for 3 h to obtain magnetic mesoporous Fe–$CaSiO_3$ materials.

The wide angle x-ray diffraction patterns were obtained on a Stoe Stadi P powder diffractometer equipped with a curved germanium (111) monochromator and linear

Table 1. Chemical composition and the reactants of mesoporous Fe–$CaSiO_3$ materials.

Sample names	Fe:Ca:Si (molar ratio)	P123 (g)	$Ca(NO_3)_2 \cdot 4H_2O$ (g)	$Fe(NO_3)_3 \cdot 9H_2O$ (g)	TEOS (g)	H_2O (ml)	HCl (ml)
0Fe–$CaSiO_3$	0:100:100	3	9.64	0	8.5	130	20.5
5Fe–$CaSiO_3$	5:95:100	3	9.15	0.82	8.5	130	20.5
10Fe–$CaSiO_3$	10:90:100	3	8.67	1.65	8.5	130	20.5

position-sensitive detector using Cu Kα1 radiation (1.5405 Å) in transmission geometry. Scanning electron microscopy (SEM) was carried out with an FEI Quanta 450 field emission scanning electron microscope. Transmission electron microscopy (TEM) was performed with a JEM-2010 electron microscope operated at an acceleration voltage of 200 kV. N_2 adsorption–desorption isotherms were obtained on a Quadrasorb SI automated surface area and pore size analyzer at −196 °C under continuous adsorption condition. Brunauer–Emmett–Teller (BET) and Barrett–Joyner–Halenda (BJH) methods were used to determine the surface area, the pore size distribution and the pore volume. Magnetic measurement was performed using a vibrating sample magnetometer.

2.2. *Ion dissolution and apatite formation of mesoporous Fe–CaSiO_3 materials in simulated body fluids (SBF)*

To investigate the ion dissolution from mesoporous Fe–$CaSiO_3$ materials, the SBF were prepared according to Kokubo's method [40]. Mesoporous Fe–$CaSiO_3$ materials were soaked in the SBF solutions at 37 °C for 1, 3, 5 and 7 days, and the ratio of mesoporous Sr–$CaSiO_3$ mass to the SBF volume was 2 mg ml^{-1}. The concentrations of the Ca, Si and Fe ions in the SBF solutions were determined by inductively coupled plasma optical emission spectrometer (ICP-OES, Shimadzu ICPS-8100). The pH values of the SBF solutions were measured after soaking mesoporous Fe–$CaSiO_3$ materials at predetermined time intervals.

The apatite formation ability of mesoporous Fe–$CaSiO_3$ materials was also carried out in the SBF solution. Typically, 0.1 g of mesoporous Fe–$CaSiO_3$ material was compacted into a pellet of 6 mm diameter by uniaxial compression at 3 MPa. Mesoporous Fe–$CaSiO_3$ pellets were soaked in the SBF solution in a polyethylene bottle at 37 °C for different periods ($M_{Fe-CaSiO3}/V_{SBF} = 2$ mg ml^{-1}). After soaking, mesoporous Fe–$CaSiO_3$ pellets were collected from the SBF solution, rinsed with ethanol and dried. SEM observations and energy-dispersive x-ray spectroscopy (EDS) measurements were used to study the apatite formation on the surfaces of mesoporous Fe–$CaSiO_3$ pellets.

2.3. *Cytotoxicity evaluation of mesoporous Fe–CaSiO_3 materials*

To investigate the cytotoxicity of mesoporous Fe–$CaSiO_3$ materials, Osteoblast-like MC3T3-E1 cells and WST-8 assay were used in this study. Prior to the cytotoxicity evaluation, the extracts of mesoporous Fe–$CaSiO_3$ materials were prepared in culture medium according to International Standard Organization (ISO/EN) 10993-5,[4] by adding mesoporous Fe–$CaSiO_3$ materials to serum-free α-MEM medium (without L-glutamine or ascorbic acid) at a final concentration of 50 mg ml^{-1}. After incubating at 37 °C for 24 h, the mixtures were centrifuged and the supernatants collected. Serial dilutions of extracts (25, 12.5 and 6.25 mg ml^{-1}) were prepared using serum-free α-MEM medium. The diluted extracts were filter sterilized and used for subsequent MC3T3-E1 cell culture experiments.

To evaluate the cytotoxicity of mesoporous Fe–$CaSiO_3$ materials, MC3T3-E1 cells were seeded at a density of 5×10^3 cells cm^{-2} into a 96-well plate with regular α-MEM medium and incubated for 24 h, after which the medium was removed and replaced by 50 μl of α-MEM medium supplemented with 20% FBS and 50 μl of diluted extracts. For a blank control, 100 μl of α-MEM medium supplemented with 10% FBS but without the addition of diluted extracts was used. The cells were incubated at 37 °C in a humidified 5% CO_2 atmosphere for 7 days. Subsequently, WST-8 (cell counting kit-8, CCK-8) assay was performed by adding 10 μl of CCK-8 solution to each well and incubated for 3 h at 37 °C to form WST-8 formazan. The absorbance of the WST-8 formazan was read at 450 nm on a microplate reader (MTP-880, Corona). The results were expressed as the absorbance reading from each well less the optical density value of a blank.

2.4. *Magnetic heating property of magnetic mesoporous Fe–CaSiO_3 materials*

For the magnetic heating experiment, a high-frequency generator (power 5 kW) was used. The used inductor was a water-cooled copper coil with 11 turns on a length of 105 mm and a diameter of 42.5 mm. For measurement, an open-top vessel with a dispersion of magnetic mesoporous Fe–$CaSiO_3$ materials (100 mg ml^{-1}) was placed in the inductor. While applying the alternating magnetic field, the temperature was monitored using a pyrometer that was placed above the inductor and focused on the dispersion surface. To obtain the heating curve of the magnetic mesoporous Fe–$CaSiO_3$ materials, a reference measurement of the pure solvent (equivalent volume) was subtracted from the data.

2.5. *Loading and* in vitro *release of gentamicin*

1.0 g of mesoporous Fe–$CaSiO_3$ materials was immersed in 40 ml of gentamicin solution (10 mg ml^{-1}). After 24 h, the drug-loaded mesoporous Fe–$CaSiO_3$ materials were separated and dried at room temperature in vacuum for 48 h. The concentration of gentamicin in mesoporous Fe–$CaSiO_3$ materials was estimated by measuring the absorbance values at 256 nm before and after the loading [41]. Before determination, a calibration curve was recorded.

In vitro release of gentamicin from the drug-loaded mesoporous Fe–$CaSiO_3$ materials was carried out with a shaking bed at 37 C. The drug-loaded mesoporous Fe–$CaSiO_3$ materials (0.5 g) were placed in a cover-sealed plastic bottle with 20 ml of the SBF solution, and the plastic bottle was fixed on a shaking bed with a shaking speed of 50 rpm. Gentamicin release was determined by UV analysis. The release medium was withdrawn at predetermined time intervals, and replaced with fresh SBF solution each time.

[4] ISO/EN 10993-5. Biological evaluation of medical devices—part 5 tests for cytotoxicity, in vitro methods: 8.2 tests on extracts.

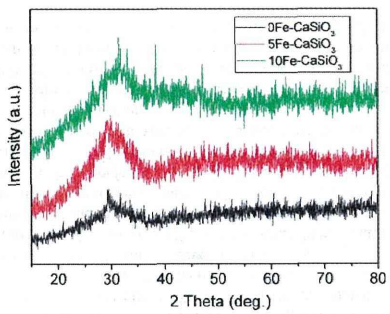

Figure 1. Wide-angle XRD patterns of mesoporous Fe-$CaSiO_3$ materials with different Fe substitution.

3. Results and discussion

3.1. *Characterization of mesoporous Fe–CaSiO_3 materials*

Figure 1 shows wide-angle XRD patterns of mesoporous Fe–$CaSiO_3$ materials. Similar to the previously reported mesoporous $CaSiO_3$, Sr–$CaSiO_3$ and magnesium–$CaSiO_3$ materials [7–9, 23, 24], mesoporous Fe–$CaSiO_3$ materials also lacked diffraction peaks related to the incorporated Fe ions except for a broad reflection at $2\theta = 25$–$35°$, which indicated the amorphous structure of Fe–$CaSiO_3$. Generally, amorphous $CaSiO_3$ has quicker apatite-formation ability due to the rapid release of Ca ions compared to α-$CaSiO_3$ and β-$CaSiO_3$ [42]. Therefore, the amorphous mesoporous Fe–$CaSiO_3$ materials could contribute to better bioactivity.

Figure 2 shows TEM images and EDS analysis of mesoporous Fe–$CaSiO_3$ materials. Well-ordered mesoporous structure can be clearly observed on mesoporous $CaSiO_3$ materials without Fe substitution (pore sizes about 5–6 nm). When 5 and 10% Fe were substituted for Ca in mesoporous $CaSiO_3$ materials, similarly ordered mesoporous channels with mesopore size of 5–6 nm could be seen, which suggested that the substitution of Fe for Ca did not change the mesoporous structure of mesoporous $CaSiO_3$ materials. From EDS analysis, Ca and Si were detected in the 0Fe–$CaSiO_3$ material, while the Fe, Ca and Si were clearly detected in the 5Fe–$CaSiO_3$ and 10Fe–$CaSiO_3$ materials, which indicated that Fe was successfully incorporated in the 5Fe–$CaSiO_3$ and 10Fe–$CaSiO_3$ materials. However, no iron oxide particles or aggregates could be detected, indicating that the Fe ions substituted the Ca ions in the framework of mesoporous $CaSiO_3$ materials, but did not form the magnetic nanoparticles inside the channels, which were similar to the previously reported results by Wu *et al* [39] and Gu *et al* [43].

Table 2. Structural parameters and gentamicin loading of mesoporous Fe–$CaSiO_3$ materials.

Samples	S_{BET} (m^2 g^{-1})	V_p (cm^3 g^{-1})	R_p (nm)	Drug loading capacity (mg g^{-1})
0Fe–$CaSiO_3$	188.1	0.233	2.68	155
5Fe–$CaSiO_3$	137.2	0.208	2.87	125
10Fe–$CaSiO_3$	134.3	0.201	3.08	124

Elemental mapping was used to further confirm the distributions of Fe, Ca and Si in mesoporous Fe–$CaSiO_3$ materials. As shown in figure 3, the chemical compositions of Fe, Ca and Si were distributed homogeneously in the 5Fe–$CaSiO_3$ and 10Fe–$CaSiO_3$ materials, which were similar to the Zr-, Mg-, Sr- and Fe-substituted mesoporous bioactive glass prepared using sol–gel technique [16, 38]. Therefore, the results further indicated that Fe ions substituted Ca ions in the framework of mesoporous $CaSiO_3$ materials. In this study, mesoporous Fe–$CaSiO_3$ materials were prepared after the calcination at 600 °C for 6 h and reduction in 10%H_2 per 90%Ar atmosphere at 400 °C for 3 h, which might form magnetite in mesoporous Fe–$CaSiO_3$. Li *et al* [44] and Chen *et al* [45] have reported that hematite could transform to magnetite in the Fe-incorporated mesoporous bioactive glasses and mesoporous silica particles after the reduction treatment under hydrogen atmosphere.

N_2 adsorption–desorption isotherms of mesoporous Fe–$CaSiO_3$ materials are shown (figure 4) together with the corresponding pore size distributions. The data for the surface area, pore volume and peak pore size are listed in table 2. The Fe substitution in mesoporous $CaSiO_3$ did not change the mesoporous structure. The type IV isotherms with a type H1 hysteresis loop were similar to those of the reported mesoporous $CaSiO_3$ materials [7, 11, 23, 24], indicating the *P6mm* mesoporous structure of mesoporous Fe–$CaSiO_3$ materials. The BET surface areas (S_{BET}) of the 0Fe–$CaSiO_3$, 5Fe–$CaSiO_3$ and 10Fe–$CaSiO_3$ materials were 188.1 137.2 and 134.3 m^2 g^{-1}, respectively. The single point adsorption total volume (V_P) at $P/P_0 = 0.97$ for the 0Fe–$CaSiO_3$, 5Fe–$CaSiO_3$ and 10Fe–$CaSiO_3$ materials were 0.233, 0.208 and 0.201 cm^3 g^{-1}, respectively. The substitution of Fe for Ca in mesoporous $CaSiO_3$ decreased the surface area and pore volume, suggesting the decrease in the ordering degree of the 5Fe–$CaSiO_3$ and 10Fe–$CaSiO_3$ materials compared to the 0Fe–$CaSiO_3$ materials. The substitution of Fe for Ca in mesoporous Fe–$CaSiO_3$ might have generated defects in the mesoporous framework due to the difference of ion valence and radius, which has been reported in the substituted mesoporous bioactive glass [16]. Previous studies

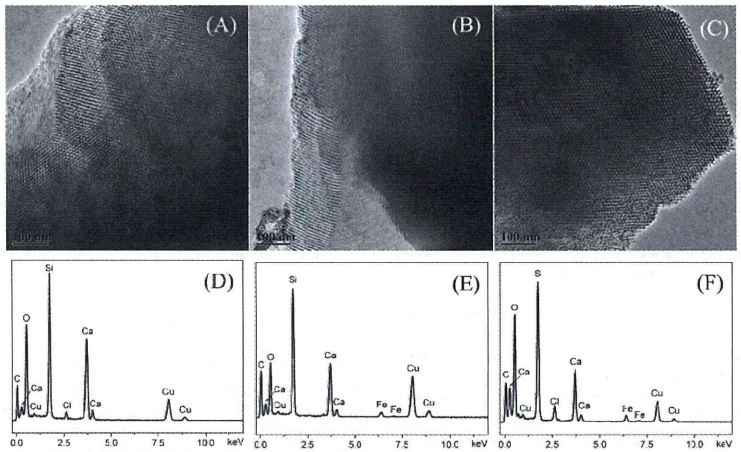

Figure 2. TEM images and the corresponding EDS analysis of mesoporous Fe-$CaSiO_3$ materials with different Fe substitution ((A) and (D): 0Fe-$CaSiO_3$; (B) and (E): 5Fe-$CaSiO_3$; (C) and (F): 10Fe-$CaSiO_3$).

have reported on the doping of Fe into glass-ceramics and Ca–P ceramics to make them magnetic, but they are unsuitable for drug delivery due to the absence of a nanoporous structure [30–33]. Furthermore, pore radius (R_P) distributions of mesoporous Fe–$CaSiO_3$ were narrow and peaked at 2.5–3 nm. In this study, the substitution of Fe for Ca in mesoporous $CaSiO_3$ materials decreased their surface area and pore volume. However, the mesoporous structure and large surface area of mesoporous Fe–$CaSiO_3$ materials ($>130\,m^2\,g^{-1}$) are beneficial for adsorption and sustained release of drugs.

3.2. Magnetic heating ability of mesoporous Fe–CaSiO$_3$ materials

The room temperature magnetization curves of the 0Fe–$CaSiO_3$, 5Fe–$CaSiO_3$ and 10Fe–$CaSiO_3$ materials are shown in figure 5(A). The magnetization of mesoporous Fe–$CaSiO_3$ materials increased with increase in Fe substitution. The 0Fe–$CaSiO_3$ materials have no magnetization due to their non-magnetic nature, whereas the 5Fe–$CaSiO_3$ and 10Fe–$CaSiO_3$ materials had a magnetization of 0.73 and 1.19 emu g^{-1} at 25 kOe, respectively, because the incorporated Fe ions formed a magnetite structure. Also, almost no hysteresis loops were observed on the curves of the 5Fe–$CaSiO_3$ and 10Fe–$CaSiO_3$ materials, suggesting superparamagnetic behavior. In practice, magnetic field generator that can operate under an AC frequency of 50 kHz–1.2 MHz and maximum magnetic field strength of 15 kA m^{-1} is considered safe for the human body [33]. In this study, the magnetic heating experiments were limited to an AC frequency of 200 kHz and magnetic field strength of 1.86 kA m^{-1}, respectively. Figure 5(B) shows the temperature increments of mesoporous Fe–$CaSiO_3$ materials in an alternating magnetic field. The 0Fe–$CaSiO_3$ suspension exhibited almost no increase in temperature during the experimental period. However, the temperatures of the 5Fe–$CaSiO_3$ and 10Fe–$CaSiO_3$ suspensions increased by 5.2 and 7.9 °C in 20 min, respectively. Therefore, the results indicated that the Fe substitution in mesoporous $CaSiO_3$ materials can produce magnetic property, and the magnetic strength of mesoporous $CaSiO_3$ materials can be tailored by changing the Fe substitution. Furthermore, magnetic mesoporous Fe–$CaSiO_3$ materials can generate heat to raise the temperature of the surrounding environment due to the delay in Neel relaxation of the magnetic moment in mesoporous Fe–$CaSiO_3$ materials [46], allowing for magnetic hyperthermia application.

3.3. Ion release and apatite formation ability of mesoporous Fe–CaSiO$_3$ materials

Studies demonstrated that the release of ions from biomaterials such as Si and Ca ions could stimulate the osteoblast proliferation and differentiation [47, 48]. On the other hand, the release of ions changes the pH around biomaterials, which will affect the cell growth and the osseointergration ability [18, 19]. Therefore, the release of Si, Ca and Fe ions from mesoporous Fe–$CaSiO_3$ in the SBF solution was investigated. As shown in figure 6, the release of Ca and Si ions increased with the increase in soaking time. However, the concentrations of Ca and Si ions decreased with increasing the Fe substitution, which might be because Fe ions provide more bonds to Si and O network than Ca ions, contributing to more stable network for mesoporous Fe–$CaSiO_3$ materials. The concentrations

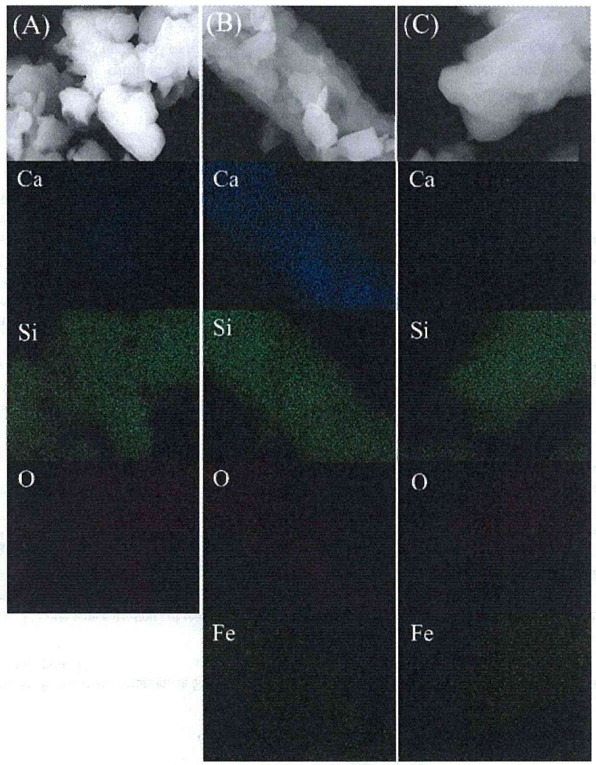

Figure 3. Element mappings of mesoporous Fe-$CaSiO_3$ materials with different Fe substitution ((A): 0Fe-$CaSiO_3$; (B): 5Fe-$CaSiO_3$; (C): 10Fe-$CaSiO_3$).

of Fe ions for the 5Fe–$CaSiO_3$ and 10Fe–$CaSiO_3$ materials were $<1\,mg\,ml^{-1}$ (not shown), which indicates that the concentration of released Fe ions was too low for ICP-OES detection. Another reason might be that the released Fe ions could be precipitated again due to the basic environment. The results were similar to those of the previously reported Fe-incorporating mesoporous bioactive glass [38, 39]. Figure 6(C) shows the pH changes of the SBF solutions after soaking mesoporous Fe–$CaSiO_3$ materials. It can be observed that the pH values of mesoporous Fe–$CaSiO_3$-soaked SBF solutions decreased with increase in the Fe substitution in mesoporous Fe–$CaSiO_3$ materials, and that the pH values could be stabilized at 8.2, 7.9 and 7.7 after 7 days of soaking for the 0Fe–$CaSiO_3$, 5Fe–$CaSiO_3$ and 10Fe–$CaSiO_3$ materials, respectively. It indicated that the substitution of Fe for Ca in mesoporous $CaSiO_3$ materials improved the ability to stabilize the pH environment, which is beneficial for cell growth on mesoporous Fe–$CaSiO_3$ materials.

It has been accepted that the apatite-formation ability of a biomaterial in SBF solution is useful for predicting the *in vivo* bone bioactivity of a biomaterial, and the formation of apatite layer shows the ability of a biomaterial to form interfacial bonds with tissues when in contact with physiological fluid [49]. In this study, the apatite formation on mesoporous Fe–$CaSiO_3$ materials after soaking in the SBF solution was investigated by SEM with EDS analysis. As shown in figure 7, after soaking mesoporous Fe–$CaSiO_3$ materials in SBF for 3 days, a new layer of apatite particles that had a diameter of several micrometers and flower morphology were formed on the surface of the pellets. Phosphorus signals appeared in the EDS spectra of mesoporous Fe–$CaSiO_3$ materials after soaking in the SBF, and the Ca/P ratio was 1.79, 1.92 and 1.95 for the 0Fe–$CaSiO_3$, 5Fe–$CaSiO_3$ and 10Fe–$CaSiO_3$ materials, respectively. The results indicated that mesoporous Fe–$CaSiO_3$ materials possess good apatite-formation ability in physiological fluid. On the other hand, it can also be